A CFD STUDY OF UCAV 1303 BASELINE MODEL AT CRUISE MACH NUMBERS

Mahmood Khalid, Weixing Yuan and Fengxian Zhang
Institute for Aerospace Research (IAR)
National Research Council Canada (NRC)
Ottawa, Ontario, Canada, K1A 0R6

Abstract

This paper furnishes further computed results for the unmanned combat air vehicle (UCAV) 1303 baseline model to be compared against the measurements provided by the Defence Science and Technology Laboratory (DSTL), UK. The subsonic/transonic computation fluid dynamics (CFD) computations were performed using both NPARC and FLOWer codes with Mach numbers M = 0.35 and 0.85 and a selection of angles of attack ranging from α = 2.0 to 18 degrees with Reynolds numbers based on a mean aerodynamic chord (MAC) of Re_{MAC} = 4.1×10⁶ and 7.2×10⁶. Comparisons between computed results were best at lower angles of attack.

1 Introduction

The UCAV 1303 type of unmanned combat aircraft will, in the future, be deployed for more dangerous missions where human pilots cannot be exposed to certain perils. These aircraft must be designed to maneuver with a precision and capability greater than those of manned aircraft. When the constraints of carrying a human pilot with limited capacity for enduring high gravitational forces are removed, such UAV combat aircraft should outperform their conventional counterparts. The pilots who will operate such vehicles from the safe environment of a remote battle station will, under a reduced stress situation, fare better against manned adversary aircraft; the latter with human cargo bombarded by countless instantaneous inputs and responses. The mission envelope for such vehicles with extended load limitations will be able to cover larger Mach and Reynolds number ranges with enhanced fatigue and limit cycle oscillation characteristics. Such vehicles will, in most circumstances, be reserved for specialized intelligence and military strike missions, with larger Global Hawk or Predator type configurations penetrating deeper into the adversary's environment to conduct longer duration surveillance and even munition deployment engagements on hard targets. These large military aircraft are ideally suited to provide important nodes of a larger communication network linking multiple theatre activities with the distributed units of a central command.

Following previous experimental and numerical simulation studies of the UCAV 1303 model, further experimental campaigns on the UCAV 1303 model were conducted in the Aircraft Research Association (ARA) transonic wind tunnels at Mach numbers M = 0.35 and 0.85. Whereas previous experimental studies involved all three leading-edge designs for the swept wings, including a rounded leading edge and a sharp pointed front profile in addition to a baseline profile, the current measurements concentrated on the baseline model only. The transition location in the experiment was fixed at 5% of the chord for both upper and lower wing surfaces, which should provide a good reference point for computed results. It was established earlier that the baseline design for the leading edge adhered best to the expected aerodynamic performance from this configuration, where the curved leading edges generate a reduced radar cross-section (RCS) signature. Other aerodynamic surfaces on the

UCAV 1303 model were designed with stealth concepts in mind. The pilot canopy merges smoothly with upper surface contours and the vehicle is designed to carry weapons inside internal bays that open at the time of munition release.

As part of an activity conducted under the auspices of The Technical Cooperation Program (TTCP), the National Research Council – Institute for Aerospace Research (NRC-IAR) recently investigated the basic aerodynamic performance of one UCAV configuration. The vehicle was shaped like a "flying wing", with a leading edge sweep angle of 45 degrees and a jagged trailing edge with a forward sweep angle of 35 degrees at the wing root. The configuration was designed principally as a stealth shape with a canopy bubble that blended smoothly with the upper surface. The numerical modeling was carried out with the NPARC Alliance [1] and FLOWer [2] codes using a number of turbulence models. The transition location was fixed at 5% of the chord for both upper and lower surfaces of the wing, as in the experiments. The subsonic freestream flow conditions were set at M = 0.35 and 0.85, and Re_{MAC} = 4.3×10^6, while the angle of attack ranged from α = 2 to 18 degrees. The computed results for the pressure distributions at various locations in the wing spanwise direction agreed well with the available measured data. While no other experimental flowfield data were available for confirmation, the computations on the UCAV configuration showed the presence of strong vortically separated flow at large angles of attack.

2 Descriptions of CFD Solvers and Grid Generation

The computations were first carried out using the NPARC Alliance solver package supplied by Arnold Engineering Development Center / National Aeronautics and Space Administration (AEDC/NASA) [1]. Two algorithms, the Beam-Warming algorithm and the multi-stage Runge-Kutta algorithm, are available in the package. The Beam-Warming algorithm [3] was selected for the present computations. This is an implicit, computationally robust scheme for solving the Navier-Stokes equations. Jameson-style artificial dissipation [4] was used to suppress the numerical oscillations and odd-even point decoupling. A number of turbulence models are available in the package. Based on past experience with configurations of similar complexity and grid dimensions [5], the Baldwin-Barth low-Reynolds-number one-equation turbulence model [6] was selected.

The code FLOWer was also applied to this exercise. The Navier-Stokes solver FLOWer [2] is a finite-volume code developed by the German Aerospace Center (DLR). The central discretization scheme proposed by Jameson et al. [4] is available. The computations reported here were based on a cell-centered formulation for the space discretization with convective fluxes evaluated using a hybrid flux vector split discretization scheme [7]. The hybrid flux vector splitting scheme switches from the advection upstream splitting method (AUSM), originally developed by Liou and Steffen [8], to the van Leer scheme [9] at shock waves, which promotes the sharp and clean shock capturing as well as the high resolution of slip lines and contact discontinuities of the AUSM. A modified monotone upstream-centered scheme for conservation laws (MUSCL) was used for second-order accuracy, which guarantees an accurate resolution of the viscous shear layers without spurious oscillations. Integration in time was performed with a Runge-Kutta scheme. The Spalart-Allmaras one-equation model [10] and Menter SST model [11] were used to model the turbulence, and were computed separately from the Reynolds-averaged Navier-Stokes equations. Roe's first-order-accurate flux-difference upwind scheme [12] was used for the convective fluxes of the turbulence equations, and a fully-implicit integration scheme was employed for the temporal discretisation. Convergence was accelerated using implicit residual smoothing and a symmetric W-type multigrid with three levels.

The structured computational grid used in this investigation was generated interactively on a Silicon Graphics workstation using ICEMCFD Hexa [13], which is a 3D object-based, semi-automatic, multi-block surface and volume mesher.

The UCAV geometry, described in [5], was meshed as a reflection-plane half model since the freestream conditions investigated do not include a sideslip angle and the resultant flow remains symmetric about a central plane. This allows the computations to be conducted with a symmetric boundary condition about the central plane. The complete flowfield can be obtained by mirroring the solution image about the central plane

A contiguous grid was generated to obtain the best communication at the interfaces between the blocks. This enables information to be directly transferable from one block to another, providing a quick and efficient solution for the entire flow domain. For the viscous flow, the grid near the surface was configured fine enough to reflect the viscous effects.

Figure 1 shows the computational mesh on the surface of the baseline model. The half-model contained 9 blocks and 4 million grid points.
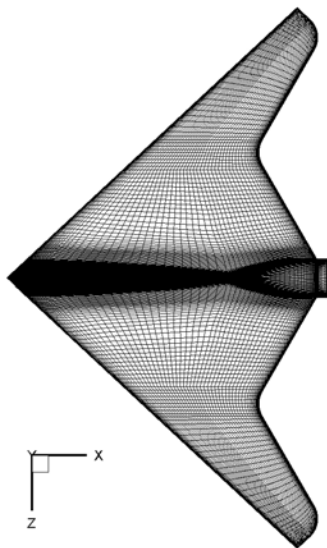
Figure 1. Illustration of the UCAV 1303 model mesh.

3 Computations and Discussion

3.1 Convergence Check and Test Cases

The first attempt using FLOWer was carried out for a flow with a freestream $M = 0.35$, $\alpha = 2.1°$, and $Re_{MAC} = 4\times10^6$. The calculations were performed using both the Jameson et al. [4] central discretization scheme and the hybrid

flux vector split discretization scheme [7], [8], [9]. The Spalart-Allmaras one-equation model [10] was selected for the turbulence modeling. When studying various results from the NPARC and FLOWer codes, the latter produced better flowfield pressure distribution comparisons against the experimental data. Therefore, the results from FLOWer were studied in more detail than those from NPARC. The convergence histories of the FLOWer calculations using the different discretization schemes are illustrated in Figure 2. The calculations based on central discretization appear to experience convergence difficulties. The flux vector splitting scheme was therefore chosen for the cases investigated in this paper.
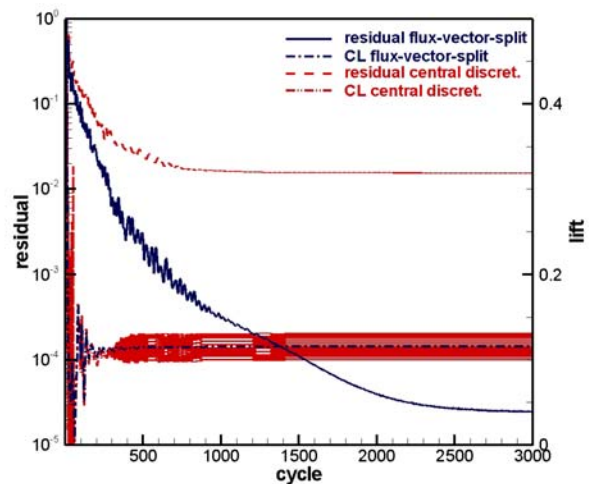
Figure 2. FLOWer convergence histories using different spatial discretizations.

To evaluate the effects of the turbulence models, in particular at high angles of attack, the Menter SST model [11] was selected for the viscous closure in the FLOWer computations. The present investigation involved four test cases, as itemized in Table 1. A direct comparison of the integrated lift and drag coefficients against measurements from DSTL [14] is also included in the same table. Without any comments on possible sources of errors from complex separated flows typical of such geometries or the absence of error bars in the experimental measurements, the comparison between the computations and experiment is quite good. One possible trend, however, is that the Spalart-Allmaras model consistently under-

predicted the lift coefficient compared to the Menter SST model.

The solution convergence histories from the above four cases are illustrated in Figure 3. While all computations demonstrate that the lift coefficient reached a steady converged level within the first 500 to 1000 iterations, the overall convergence patterns, while equally satisfactory, show that calculations with the Spalart-Allmaras model were slightly more efficient.

3.2 Pressure Distributions

Figure 4 shows the pressure distribution computed using NPARC and FLOWer at M = 0.35, Re_{MAC} = 4.1×10^6 and α = 2.1° compared against experimental data from DSTL UK [14]. At this low angle of attack, the comparison at spanwise locations of η = 0.3, near the wing root, and 0.6, farther outboard, was quite good. At a higher angle of attack, α = 5.9°, with the same Mach and Reynolds number conditions, the comparison at η = 0.3, shown in Figure 5, was quite good, but the comparison at η = 0.6 was somewhat inconclusive. It appears that NPARC was not able to resolve the suction peak as successfully as FLOWer, which continued to perform better beyond the suction peak near the upper forward regions of the wing. The experimental data include an inexplicably odd pressure point near x/c = 0.275 for this spanwise location that may not be representative of the actual physics.

At a still higher angle of attack, α = 10°, for the same Mach and Reynolds number conditions, the pressure distribution shown in Figure 6 for the upper forward regions near the wing root, η = 0.3, was reasonably well predicted by the NPARC code. There was even a reasonable attempt by the code to capture the suction peak. At the outward spanwise location, η = 0.6, the flowfield described by the pressure streamline traces in the flow visualizations (see the next Section) was separated right from the leading edge vortex. Under these conditions, it is difficult for most turbulence models to recover the flow accurately. Thus, both codes failed to resolve the flow adequately at this location.

At transonic flow conditions Figure 7, M = 0.85, Re_{MAC} = 7.1×10^6, and α = 2.1°, both codes produced satisfactory comparisons against the experimental data. While the agreement was quite good for the location near the wing root, η = 0.3, the limited measured data were insufficient to formulate a general conclusion. The comparison near η = 0.6 was satisfactory. Here, NPARC out-performed FLOWer both in terms of the overall pressure distribution agreement as well as the location of the shock on the upper surface.

3.3 Flow Visualizations

Flow visualization studies of the various computed cases were conducted to facilitate interpretation of the computed results and the experimental data. The results indicated that the flow state for this configuration was not easy to resolve at larger angles of attack.

At lower angles of attack, α = 2.1º and 5.9º, as noted in Figure 8 and Figure 9, the flow was mostly attached; thus, the turbulence models were successful at solving this configuration. For most loadings and steady longitudinal stability and control studies, the NPARC and FLOWer codes can be relied upon to come up with reasonable estimates of the performance design coefficients. Even under transonic conditions, as depicted in Figure 11, the solvers did an adequate job of predicting the shock location at lower angles of attack (α = 2.1°).

However, at higher angles of attack, α= 10º, shown in Figure 10, the leading edge gave rise to a strong vortex that spread across the entire wing beyond the 50% spanwise station. The vortex had a tendency to lift the flow from the surface, giving rise to a complex three-dimensional separation that is quite problematic for most turbulence models to resolve.

4 Conclusions

Since an UCAV geometry has to achieve a balance between the complex demands of aerodynamics and radar signatures and has the added imperative to hide all armaments in internal cavities, the resulting complex blended wing-body geometry shape is fraught with aerodynamic challenges. The varying convex spanwise sections promote strong three-dimensional effects and create a leading edge vortex at higher angles of attack, which appears to be responsible for promoting separation towards the outboard portions of the wing.

The current computations show that at lower angles of attack, $\alpha \leq 5.9^\circ$, the flow can be solved using state-of-the-art viscous solvers and standard turbulence models. At higher angles of attack, near 10 $^\circ$, that turbulence models such as the Baldwin-Barth, Spalart-Allmaras, and Mentor SST models, are not able to resolve the complexity of the separated flows. With these external flow fields, such blended wing-body configurations will have even more complex aero-acoustic signatures when equipped with embedded cavities to accommodate armaments.

Acknowledgments

References

[1] The NPARC Alliance. *NPARC User's Guide*. Version 3.0, Sep. 1996.

[2] Kroll N, Rossow C C, Schwamborn D, Becker K and Heller G. MEGAFLOW – A Numerical Flow Simulation Tool for Transport Aircraft Design. *ICAS Congress*, Toronto, Canada, Paper No. 1105, 2002.

[3] Beam R and Warming R F. An Implicit Finite Difference Algorithm for Hyperbolic Systems in Conservation Law Form. *Journal of Computational Physics*, Vol. 22, No. 1, pp. 87-110, Sep. 1979.

[4] Jameson A, Schmidt W and Turkel E. Numerical Solutions of the Euler Equations by Finite Volume Methods Using Runge-Kutta Time-Stepping Schemes, *AIAA* Paper 81-1259, 1981.

[5] Zhang F, Khalid M and Ball N. A CFD Based Study of UCAV 1303 Model. *23rd AIAA Applied Aerodynamics Conference*, Toronto, Canada, June 6 – 9, 2005.

[6] Baldwin B S and Barth T J. *A One-Equation Turbulence Transport Model for High Reynolds Number Wall-Bounded Flows*. NASA TM 102847, Aug. 1990.

[7] Kroll N and Radespiel R. *An Improved Flux Vector Split Discretization Scheme for Viscous Flows*. DLR Report, German Aerospace Centre, Braunschweig, DLR-FB 93-53, 1993.

[8] Liou M S and Steffen Ch. A New Flux Splitting Scheme. *Journal of Computational Physics*, Vol. 107, No. 1, pp. 23-39, 1993.

[9] van Leer B. Flux vector Splitting for the Euler Equations. *Lecture Notes in Physics*, Vol. 170, pp. 507-512, Springer-Verlag, 1982.

[10] Spalart P R and Allmaras S R. A One-Equation Turbulence Model for Aerodynamic Flows. *30th Aerospace Sciences Meeting and Exhibit*, Reno, AIAA-92-0439, 1992.

[11] Menter F R. Two-Equation Eddy-Viscosity Transport Turbulence Model for Engineering Applications. *AIAA Journal,* Vol. 32**,** pp 1598-1605, 1994.

[12] Roe P L. Approximate Riemann Solvers, Parameter Vectors and Difference Schemes, *Journal of Computational Physics*, Vol. 43, pp. 357-372, 1981.

[13] http://flash.icemcfd.com/index.html.

[14] Bruce R J. *High Speed Wind Tunnel Tests on the 1303 UCAV Concept*. Internal Report, QinetiqQ Ltd, QinetiqQ Farnborough, UK, QINETIQ/FST/TR030214/1.0, 2003.

Copyright Statement

Table 1 Summary of computational cases

Case	M	Re	α	CL			CD		
				SA	SST	Exp.	SA	SST	Exp.
1	0.35	4.1M	2.1°	0.115	0.118	0.117	0.00798	0.00818	0.00957
2	0.35	4.1M	5.9°	0.311	0.321	0.314	0.0248	0.0250	0.0184
3	0.35	4.1M	10°	0.509	0.531	0.541	0.0709	0.0722	0.0678
4	0.85	7.1M	2.1°	0.142	0.159	0.162	0.0109	0.0111	0.0118
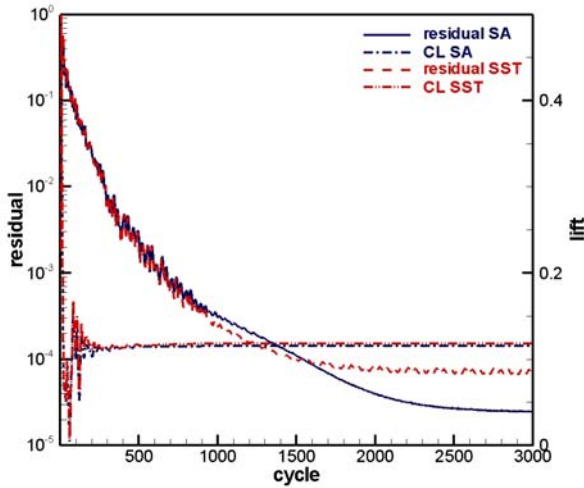
Case 1: M = 0.35, Re_{MAC} = 4.1×10^6, α = 2.1°
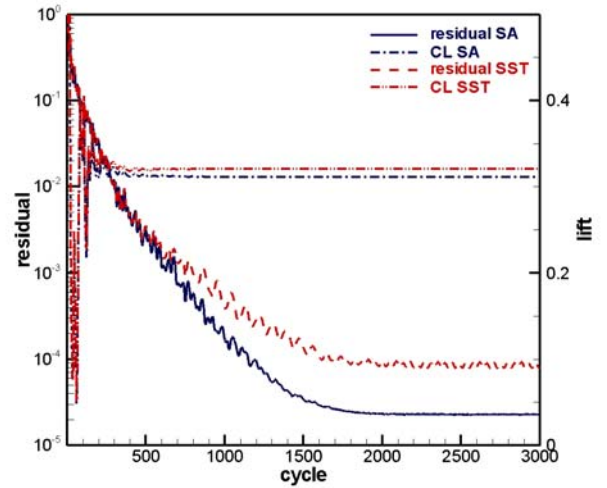
Case 2: M = 0.35, Re_{MAC} = 4.1×10^6, α = 5.9°
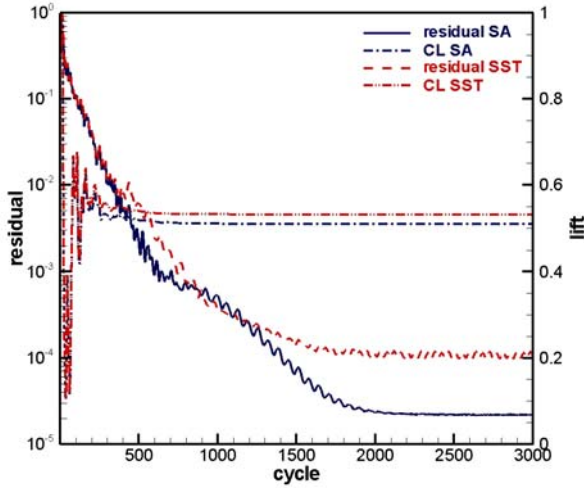
Case 3: M = 0.35, Re_{MAC} = 4.1×10^6, α = 10°
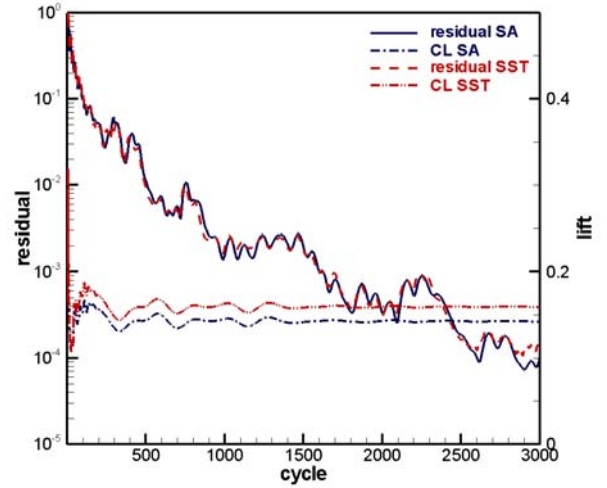
Case 4: M = 0.85, Re_{MAC} = 7.1×10^6, α = 2.1°

Figure 3 Convergence histories of FLOWer computations using different turbulence models.

η = 0.3   η = 0.6
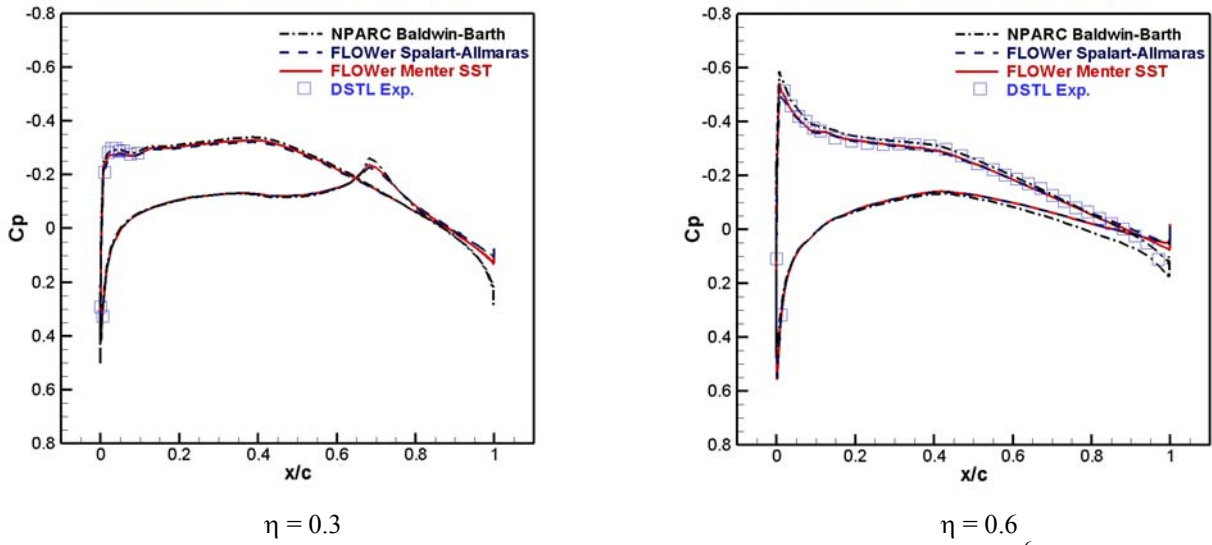
Figure 4 Comparison of CFD results against experiment at M = 0.35, Re = 4.1 ×10^6, α = 2.1°.

η = 0.3   η = 0.6
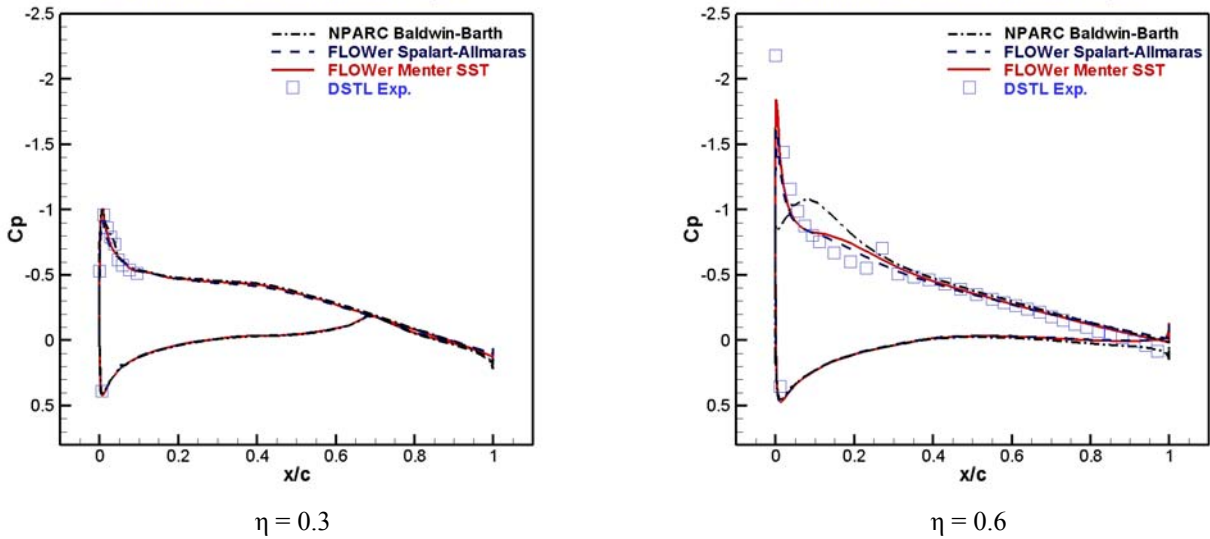
Figure 5 Comparison of CFD results against experimental data at M = 0.35, Re$_{MAC}$ = 4.1×10^6, α = 5.9°.

η = 0.3   η = 0.6
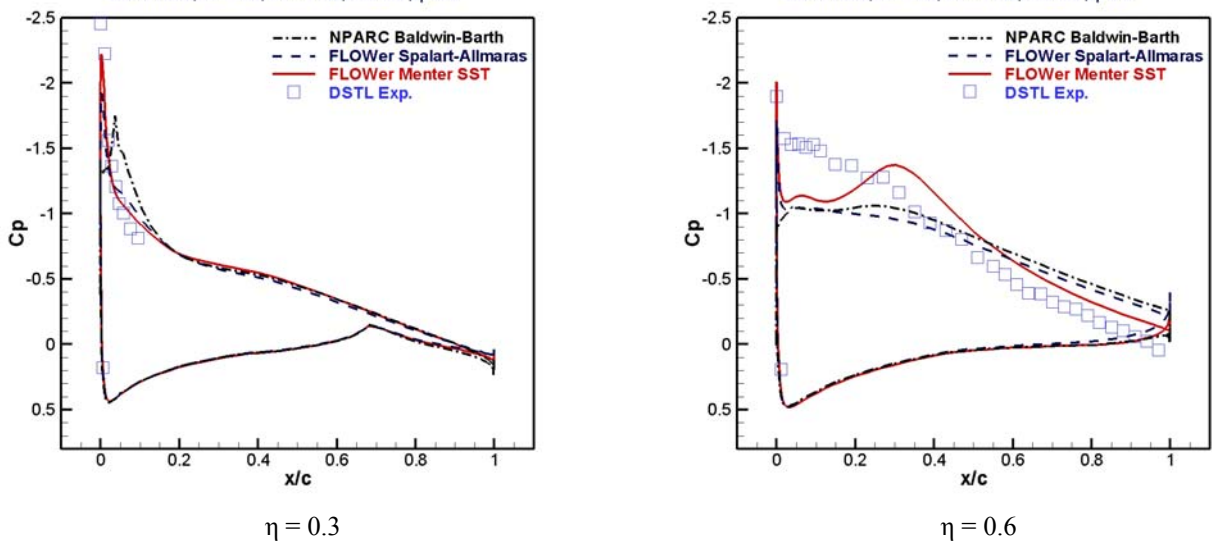
Figure 6 Comparison of CFD results against experimental data at M = 0.35, Re$_{MAC}$ = 4.1×10^6, α = 10°.

η = 0.3
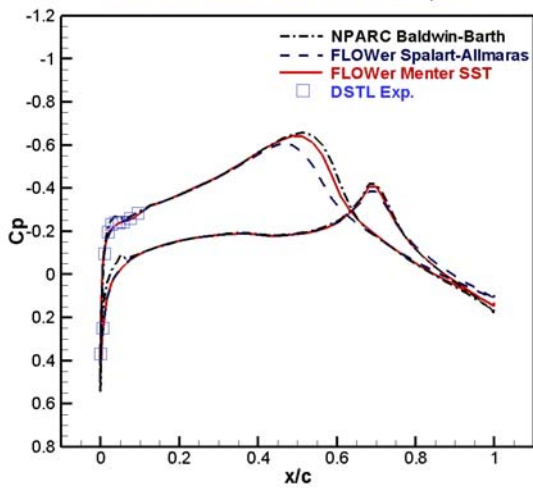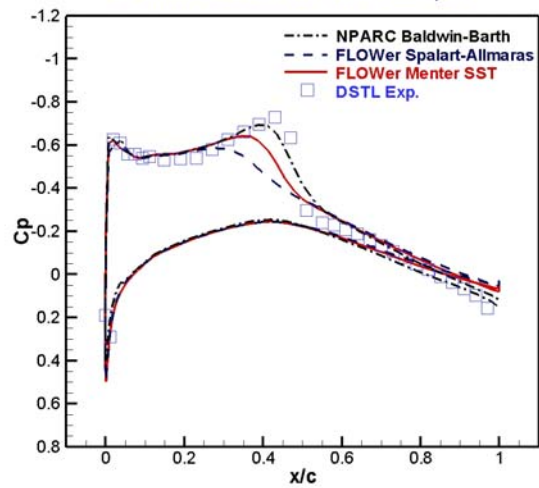
η = 0.6

Figure 7 Comparison of CFD results against experimental data at M = 0.85, Re_{MAC} = 7.1×10⁶, α = 2.1°.
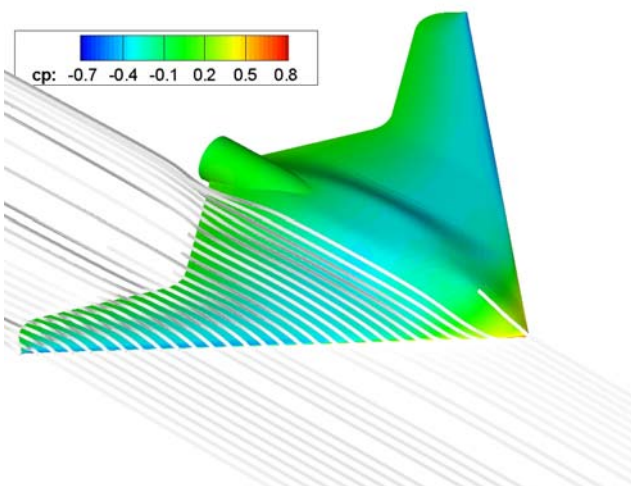
FLOWer with Spalart-Allmaras model
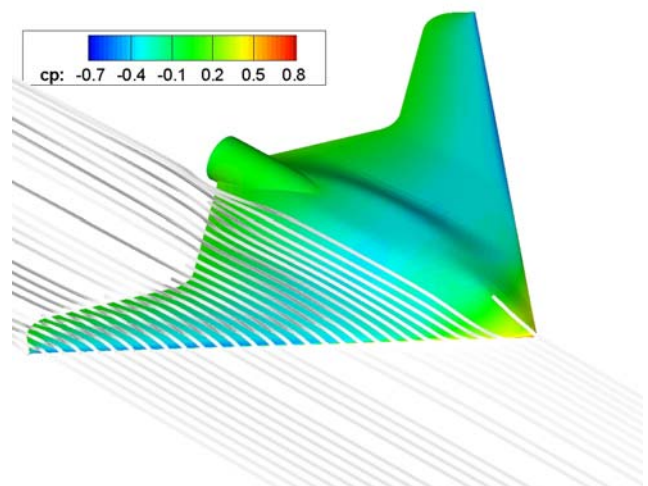
FLOWer with Menter SST model
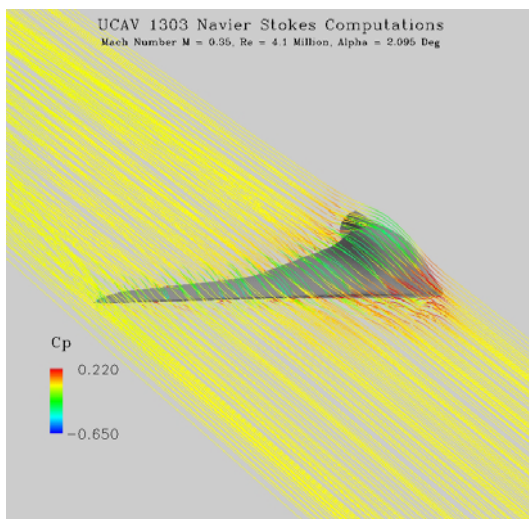
NPARC with Baldwin-Barth model

Figure 8 Computed flowfield at M = 0.35, Re_{MAC} = 4.1×10⁶, α = 2.1°.

Spalart-Allmaras model
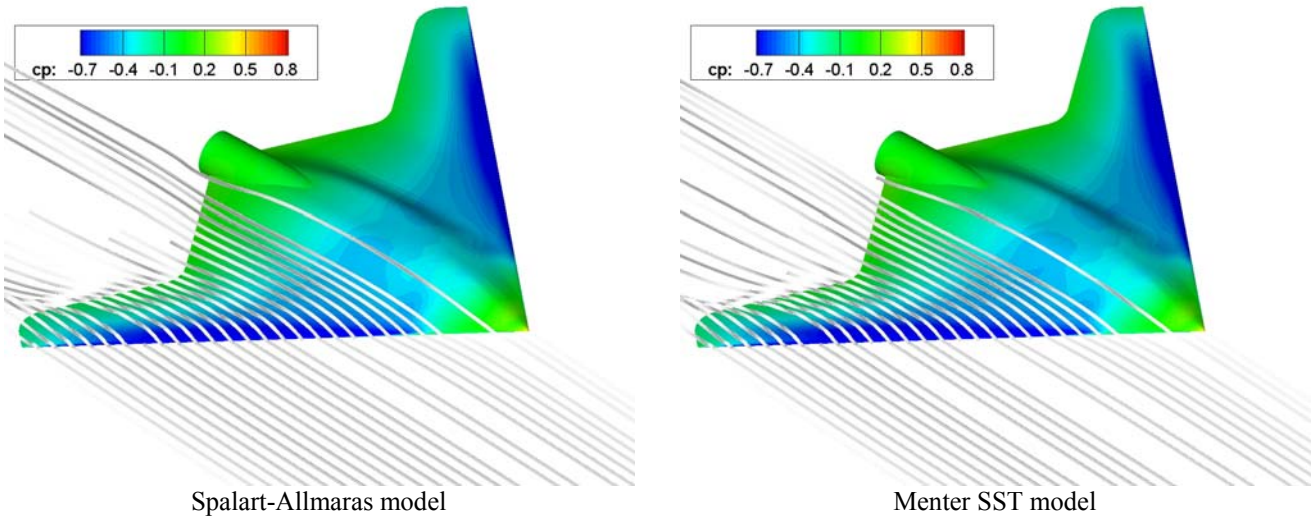
Menter SST model

Figure 9 Computed flowfield at M = 0.35, Re$_{MAC}$ = 4.1×10^6, α = 5.9°.

FLOWer with Spalart-Allmaras model

Menter SST model

Baldwin-Barth model
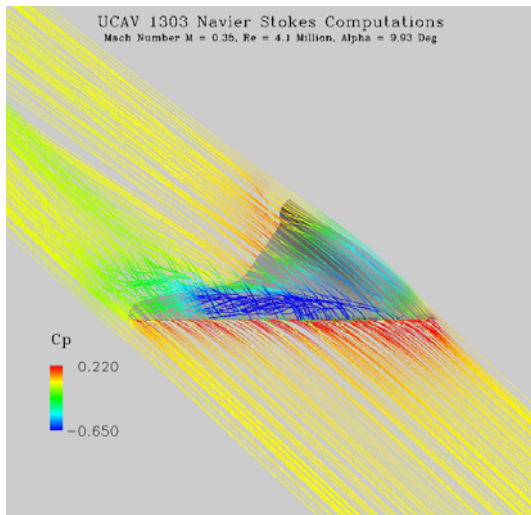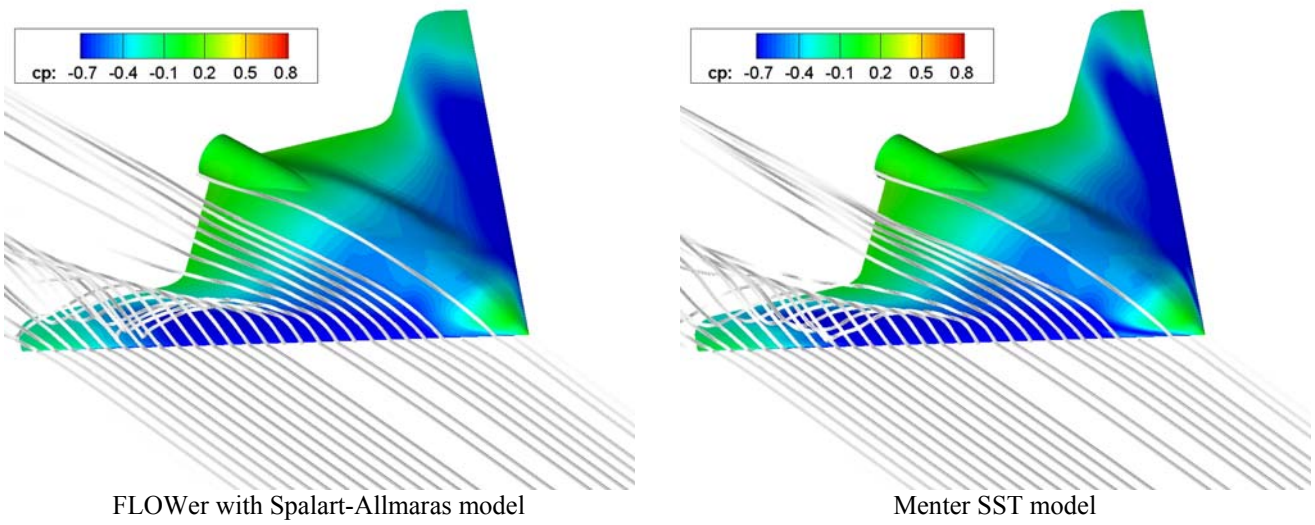
Figure 10 Computed flowfield at M = 0.35, Re$_{MAC}$ = 4.1×10^6, α = 10°.
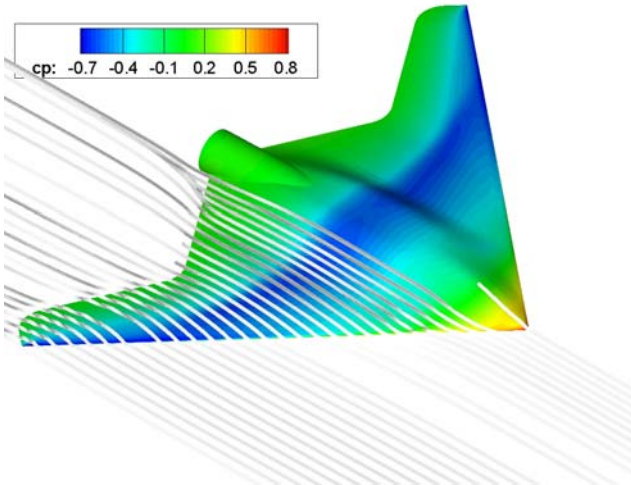
NPARC with Spalart-Allmaras model
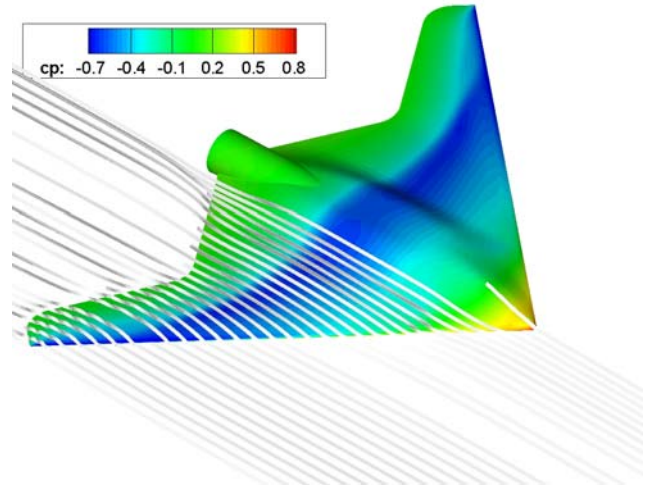
FLOWer with Menter SST model
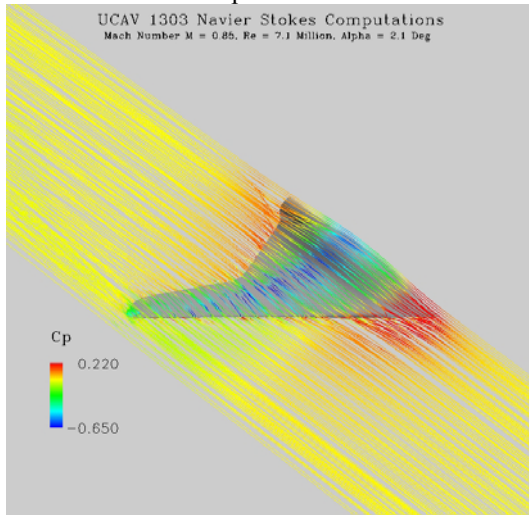
Baldwin-Barth model

Figure 11 Computed flowfield at M_{MAC} = 0.85, Re = 7.1×10^6, $\alpha = 2.1°$.